1 **Hydrodynamics of the frontal strike in aquatic snakes: drag, added mass and the**

2 **possible consequences for prey capture success.**

3 Marion Segall*[1,2,3], Anthony Herrel[1,4] and Ramiro Godoy-Diana[2].

4 1. UMR CNRS/MNHN 7179, « Mécanismes adaptatifs et Evolution », 55 Rue Buffon,
5   75005, Paris, France.
6 2. Laboratoire de Physique et Mécanique des Milieux Hétérogènes (PMMH), UMR
7   CNRS 7636 ; ESPCI Paris, PSL Research University, Sorbonne Université,
8   Université Paris Diderot, 75005 Paris, France.
9 3. Department of Herpetology, American Museum of Natural History, Central Park
10   West at 79th Street, New York, NY 10024.
11 4. Evolutionary Morphology of Vertebrates, Ghent University, K.L. Ledeganckstraat
12   35, B-9000 Ghent, Belgium.

13 Corresponding author: Marion Segall, marion.segall@live.fr

14 *Running title:* Hydrodynamics of snake prey capture

15 *Summary statement:* The present work explores the functional implications of head shape

16 in a group of aquatic predators using a fluid mechanics approach.

Abstract

Natural selection favors organisms that are the most successful in fitness-related behaviors such as foraging. Secondary adaptations pose the problem of re-adapting an already 'optimized' phenotype to new constraints. When animals forage underwater, they face strong physical constraints, particularly when capturing prey. Successful prey capture requires a predator to be fast and to generate a high acceleration. This involves two main constraints due to the surrounding fluid: drag and added mass. Both constraints are related to the shape of the animal. We experimentally explore the relationship between shape and performance in the context of an aquatic snake strike. As a model, we use two different 3D-printed snake heads representing typical shapes of aquatically-foraging and non-aquatically-foraging snakes, and frontal strike kinematics based on *in vivo* observations. By using direct force measurements, we compare the drag and added mass faced by the aquatic and non-aquatic snake models during a strike. Our results show that both drag and added mass are optimized in aquatic snakes. Using flow field measurements with particle image velocimetry, we examine the fluid dynamical mechanisms that could be behind the reduction of hydrodynamic constraints observed for the aquatic snake head shape, which makes it well suited to capture prey under water.

Key words: snakes, fluid mechanics, forces, morphology, prey capture

Introduction

Aquatic animals have to overcome the strong viscous and inertial constraints associated with underwater movement [1]. Physically, these constraints are related to the kinematics of movement and the morphology of an animal (i.e. the shape of the object that is facing the flow). For most aquatic vertebrates, viscous effects are confined to a thin boundary layer surrounding the body, which couples the motion of the animal with that of the surrounding fluid and gives rise to the skin friction that penalizes aquatic locomotion. In addition, fluid inertia causes the boundary layer to separate from the animal's body, creating the recirculation zones associated to pressure drag [2]. The specifics of the flow separation determine the relative importance of pressure to skin friction drag [3,4]. In addition to drag, which depends on the velocity of the animal, the hydrodynamics are also dependent on acceleration of the added mass [5,6]. This corresponds to the mass of fluid that is accelerated together with the animal and which exerts a reaction force. Both drag and added mass depend on the size and shape of the body [5], and it can thus be expected that the morphology of aquatic animals has evolved to reduce drag and added mass. However, organisms have a morphology that is also constrained by evolutionary history, functional trade-offs, and developmental programs thus restricting the range of possible morphological adaptations. Environmental and biological constraints act simultaneously on an organism and may all impact their evolution, sometimes leading to convergent phenotypes [7–10]. Morphological convergence is common across the animal kingdom, yet its impact on function has only rarely been tested [11–15]. We here use the case of convergence in head shape in aquatic snakes [16] to provide an experimental test of the suggested functional advantages of observed similarities in the head shape of aquatic snakes.

Snakes are an ideal model to study convergence as they have invaded the aquatic medium multiple times independently throughout their evolutionary history. However, they do not show any of the usual adaptations to aquatic prey capture (e.g. they cannot perform suction feeding due to their reduced hyoid [14]). Snakes have to deal with the hydrodynamic constraints when capturing a prey, and as these constraints are related with the shape [1,13,17], the head of aquatically foraging snakes should have evolved in a way to minimize the constraints. Convergence in head shape in aquatic snakes has been demonstrated previously [14–16,18,19]. In a previous work [16], we compared the head shape of 62 species of snakes that capture prey under water (from sea snakes over homalopsids to North American watersnakes) versus 21 phylogenetically closely related species that do not forage under

68   water. We used 3D geometric morphometrics on surface scans of these species and ran

69   phylogenetic analyses demonstrating a morphological convergence in head shape of

70   aquatically foraging snakes. Moreover, we characterized the shapes that are specific of both

71   group of snakes (i.e. the aquatic and the non-aquatic foragers). We hypothesized that the

72   convergent shape would provide a hydrodynamic advantage to aquatic foragers in

73   comparison with their close relatives that do not capture aquatic prey. Several previous

74   studies similarly have suggested convergence to give rise to a functional advantage [13,14,16,20],

75   yet this has never been tested experimentally. Thus, we here propose an experiment to test

76   this idea. In other words, we investigate whether the head shape associated with aquatically

77   foraging snakes has a hydrodynamic advantage over the shape associated with the non-

78   aquatic foragers. The hydrodynamic constraints involved during a strike are the pressure

79   drag – skin friction being negligible in the regimes of interest here [11] – and the added mass.

80   Both of these constraints are related to a certain extent to the shape of the object that is

81   moving through a fluid [5,6]. Thus, if our hypothesis is correct, the shape corresponding to the

82   aquatic forager should show less drag and added mass than the non-aquatic model.

83   Another constraint related to the capture of prey under water is the

84   mechanosensitivity of aquatic prey like fish. The lateral line system of fish is composed of

85   mechanoreceptors that can detect very small pressure variations with an estimated threshold

86   of 0.1 to 1 mPa at 1 mm [21,22]. This system triggers a reflex escape response in the prey once

87   a pressure threshold has been reached. Previous studies have suggested that a snake moving

88   underwater generates a bow wave that might be able to trigger the reflex response of the prey

89   [11,14]. We tested this hypothesis and predicted that aquatic snakes should be stealthier than

90   non-aquatic snakes during the strike such that the detection of the predator by the prey would

91   be delayed.

92   We use direct force measurements on two 3D printed models of snake heads derived

93   from our previous work based on the comparison of 83 species of snakes [16] (i.e. more than

94   400 snake specimens). As these models results from a 3D geometric morphometric analysis,

95   the models are scaled to the same size, allowing us to specifically test for the impact of shape

96   on hydrodynamic constraints. Our experimental setup mimics a 'sit-and-wait' frontal strike

97   under water, meaning that the model remains motionless before the strike and is then

98   suddenly accelerated to reach an almost constant speed for a short time. We compared

99   models with the mouth open, as aquatic snakes keep their mouth opened during frontal

100 strikes (Fabre et al., 2016; van Netten, 2006; Vincent et al., 2009, Herrel and Segall pers

101   obs.). The force applied to the head during the strike was recorded to characterize the added

102   mass and drag, which determine the hydrodynamic efficiency of a strike. In addition, another

103   sensor was placed at the end of the strike track to assess the distance at which a prey is likely

104   to detect the presence of the snake during capture. Particle Image Velocimetry (PIV) was

105   used to visualize the flow field around the head during a strike. We also characterized the

106   evolution of the vortex intensity during a strike for each shape, as it is closely related to the

107   hydrodynamic forces generated by a moving object [23–25].

108   **Material & Methods**

109   *3D models*

110   We compared two models that we termed "aquatic" and "non-aquatic" (Fig. 1). These

111   shapes result from a 3D geometric morphometric study showing that the head shape of

112   aquatic snake species has converged, possibly in response to the hydrodynamic constraints

113   involved during prey capture under water [16]. We compared the hydrodynamic forces that are

114   exerted on each of the head shapes during a simulated capture event. The geometric

115   morphometric analysis allows to extract shapes independent of variation of size such that the

116   shapes are directly comparable to one another. In a next step we opened the mouth of the

117   models as snake use to attack their prey with the mouth open. We used Blender™ to rotate

118   the jaw and the top of the head to reach an angle of 70° based on previously published data

119   on frontal strikes in snakes [14,26,27]. The two models were then 3D printed using a Stratasys

120   Fortus 250 MC 3D printer with ABS P430 as a material (Fig. 2a.).

non-aquatic model   aquatic model
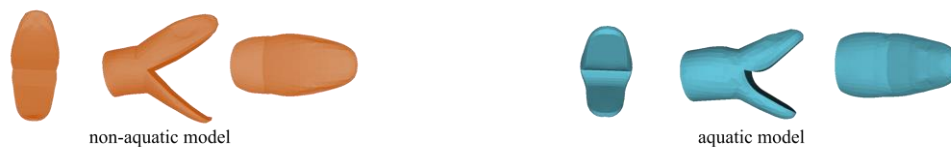
121

122   *Figure 1: 3D models of the head shape of non-aquatic (left) versus aquatic snakes (right)*

123   *in front, side and top view.*

124   *Experimental setup*

125   Snakes capture their prey using high acceleration forward motions that we mimicked

126   using springs (Fig. 2a). We generated a range of speeds and accelerations by applying a

127   different compression on the spring. We used a force sensor FUTEK LSB210+/-2 Lb to

128 record the force exerted on the models which were positioned horizontally inside a water

129 tank. This sensor was attached to the model using an aluminum rod and recorded the axial

130 forces applied to the head during a strike. The other side of the sensor was attached to a

131 bracket (sensor 1, Fig. 2a) that was itself hooked on the movable part of an air-bearing rail

132 that allows the system to remain frictionless. This movable part was compressed against the

133 spring and suddenly released. The length of the path was 20cm. Approximately 60 trials (i.e.

134 spring compressions) were done for each model. To obtain the kinematics of each strike, we

135 recorded the position of the movable part using a position sensor (optoNCDT1420, Micro-

136 Epsilon) (Fig. 2a).

137   In addition, we wanted to assess what a prey would sense in terms of pressure, so we

138 placed another, more sensitive, force sensor (FUTEK LSB210 100 g) at the end of the path

139 to which we attached a round plastic piece of diameter 7 cm that allowed us to record the

140 pressure changes (sensor 2, Fig. 2a). This sensor provided information about the distance at

141 which a prey could potentially detect the presence of a snake during a strike. The force and

142 position sensors were synchronized, and data were recorded at 1 kHz.

143

6
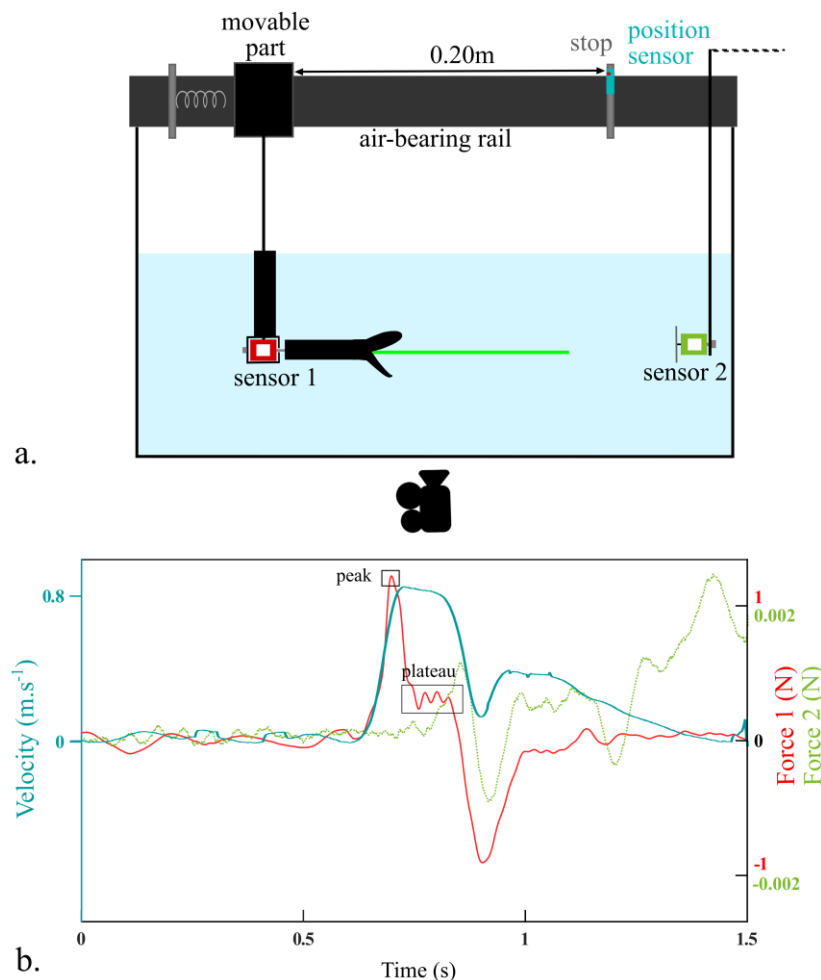
144 *Figure 2: a. Experimental setup used to simulate a frontal attack of a snake towards a*

145 *prey. b. Example of the output of the force sensor 1 (red line), force sensor 2 (green dashed*

146 *line) and velocity (blue line) during one trial (i.e. one strike). The plateau and peak force*

147 *used to calculate the hydrodynamic forces are indicated.*

148   *Drag coefficient and added mass*

149   The first part of the strike is the acceleration phase during which the velocity

150 increases. This phase corresponds to the decompression of the spring. It is correlated with a

151 dramatic increase in the force that is applied to the snake head model (red line, sensor 1, Fig.

152 2). Once the springs are completely decompressed, the system is no longer accelerating, and

153 the velocity decreases slowly. In parallel, the force applied to the model decreases until it

154 reaches a plateau-like phase (Fig. 2b). Then, the system hits the stop at the end of the track

155 and moves backward generating a large drop in both velocity and force signaling the end of

156 the trial.

157   During the plateau phase (Fig. 2b), the only force that is applied to the model and

158 thus, the only force that is recorded by the sensor is the drag force. Thus, we used the average

159 force recorded during this phase (F_d) to calculate the drag coefficient (C_d) of both of our

160 models by using the standard definition [2]:

$$C_d = \frac{2F_d}{\rho U^2 S} \qquad (1)$$

162 where F_d is the drag force, ρ is the density of water, U the velocity of the object and S its

163 projected frontal surface area, which was measured at 12.89 cm² for the aquatic model and

164 14.72 cm² for the non-aquatic model. The term $2F_d/\rho S$ was plotted against U^2 and the linear

165 regression coefficient corresponds to the drag coefficient of the models (Fig. 3). The

166 Reynolds number range of our experiments is 1.10^4-7.10^4.

167   During the acceleration phase, both drag and inertial forces are at play, meaning that

168 the peak force (F_{peak}, Fig. 2b) recorded by the force sensor is composed of these two forces.

169 To calculate the added mass generated by both models, we used the following calculation

170 steps for each trial, we first calculated the inertial force by subtracting the instantaneous drag

171 force from the peak force measured by the sensor:

$$F_i = F_{peak} - F_{d(t1)} \qquad (2)$$

7

173   where F_i is the inertial force applied to the model and $F_{d(t)}$ is the instantaneous drag force

174   when the acceleration reaches its maximum:

175
$$F_{d(t1)} = \frac{1}{2}\rho U_{(t1)}{}^2 C_d S \quad (3)$$

176   Here ρ is the density of water, $U_{(t1)}$ the velocity at the instant the acceleration is maximal

177   and S the projected frontal surface area of each model. Now, the added mass M can be

178   computed as:

179
$$M = \frac{F_i - ma}{a} \quad (4)$$

180   where m is the mass of the object, and a the acceleration.

181   Finally, the added mass coefficient (C_a) [2]:

182
$$C_a = \frac{M}{\rho V} \quad (5)$$

183   where V is the volume of the model: $7.33.10^{-5}$ m^3 for the aquatic model and $5.78.10^{-5}$ m^3 for

184   the non-aquatic model.

185   The added mass coefficient was obtained by plotting the added mass term $(F_i - ma)/\rho V$,

186   against the acceleration (a). The linear regression coefficient corresponds to the added mass

187   coefficient of the models (Fig. 4).

188   *Detection distance*

189   To compare the effect of the head shape on the detection by a possible prey we used

190   the output of the second force sensor (sensor 2, Fig. 2a). This sensor can detect pressure

191   variations of approximately 0.3 Pa which is around the hearing and the startle threshold of

192   some fish (i.e. between 0.01Pa and 0.56Pa) [28,29]. To estimate the position at which the prey

193   could detect the predator, we defined the detection distance d as the position at which the

194   force detected by sensor 2 deviates from the unperturbed value by more than one standard

195   deviation of the sensor output before the strike (green dashed line, Fig 2b, Fig. 5).

196   *Particle Image Velocimetry*

197   We used 2D Particle Image Velocimetry (PIV) with a high-speed camera, Dantec

198   Dynamics SpeedSense M, to obtain a time-resolved recording of the strike from the bottom

199 of the tank (Fig. 2a.). Water was seeded with polyamid particles of 20 μm in diameter and a

200 Quantronix® Darwin-Duo laser was used to produce the light sheet. Image acquisition was

201 performed at 733Hz. We choose to record three different planes on each head to obtain a

202 complete picture of the fluid flow around the head during the attack (see Supplementary Fig.

203 S1). We applied the same compression to the springs (i.e. maximal compression) to get an

204 equivalent comparison for the different shapes. Acquisition was performed using the Dantec

205 DynamicStudio 2015a software. The PIV vector computation was performed using LaVision

206 7.2 with a 16 x 16 pixel^2 interrogation window and 50% overlap. Additional post-processing

207 and analysis was done in Matlab using the PIVMat toolbox [30]. A more quantitative analysis

208 was performed by computing the overall primary circulation $\Gamma = \int \omega^+ dA$ in each PIV plane

209 (ω^+ being the positive vorticity in Fig. 6b.). The evolution of the dimensionless circulation

210 Γ/UL as a function of time, where L is the characteristic length scale of the acceleration

211 regime of the strike maneuver (which is constant for all experiments) and U is the velocity

212 of the strike is plotted in Fig. 6b.

213 *Statistical analyses*

214   To test for differences between the drag coefficients of the two shapes, we ran a

215 Pearson correlation on the force component of the drag coefficient ($2F_d/\rho S$) with the square

216 velocity (U^2). An ANCOVA with mass as a co-variate was performed to test for statistical

217 differences in the drag coefficient between the two models. To compare the detection

218 distance, we ran an ANCOVA with the distance as the response variable, the model as a

219 factor, and the velocity as covariate. All the variables were Log$_{10}$-transformed and the

220 statistical analyses were performed using R [31]. The significance level was set at 5%.

221 **Results**

222 *Drag and added mass*

223   The drag coefficient of the non-aquatic shape is higher than the coefficient of the

224 aquatic model, respectively 0.64 and 0.26 (Pearson's correlation: nonaq: df = 67, $P < 0.001$,

225 R^2 = 0.996; aq: df=64, $P < 0.001$, R^2 = 0.995; ANCOVA: $F_{2,132} = 671.1$, $P < 0.001$) (Fig. 3).
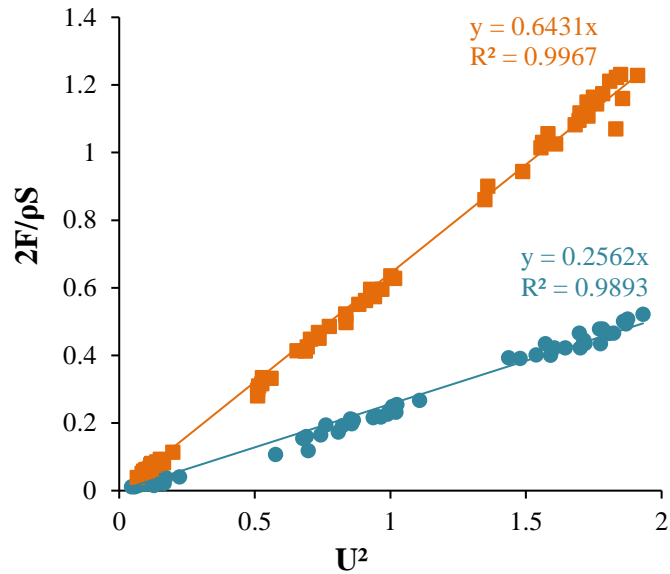
9

226

Figure 3: Drag term $2F_d/\rho S$ depending on the velocity term of the strike (U^2) for the two head models tested. Linear regression lines are drawn. The slopes correspond to the drag coefficient of each shape and the R^2 are the regression coefficients. Squares: non-aquatic model, circles: aquatic model.

The mean added mass obtained is 12.67 g for the aquatic model versus 14.95 g for the non-aquatic model. The added mass coefficients obtained from the linear regression on Fig. 4 are 0.151 for the aquatic model and 0.235 for the non-aquatic model.
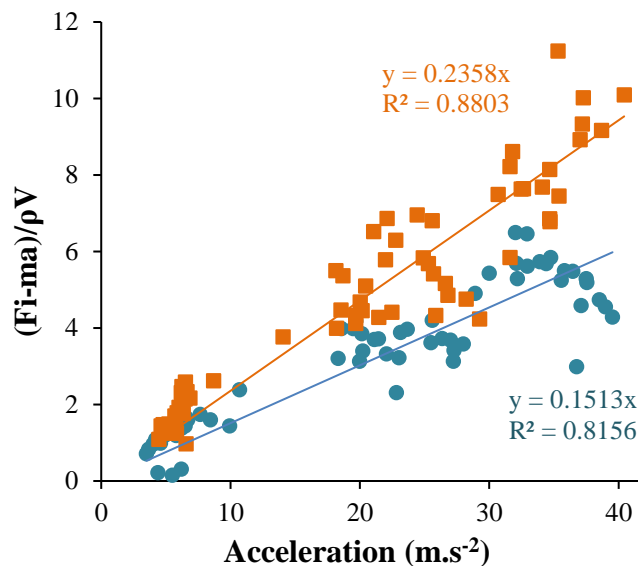

234

Figure 4: Normalized inertial force term $(F_i - ma)/\rho V$ depending on the acceleration of the strike (a in m.s^{-2}) for the two head models tested. Linear regression lines are drawn.

10

237   *The slopes correspond to the added mass coefficient of each shape and the R^2 are the*

238   *regression coefficients. Squares: non-aquatic model, circles: aquatic model.*

239   *Detection distance*

240   The force signal was too noisy to get any accurate measures of the detection distance

241   at low velocities (i.e. $U > 0.5$ m.s^{-1}). There is moreover no statistical difference between the

242   distances at which the prey could detect the presence of the snake depending on their head

243   shape. However, this distance depends on the maximal velocity of the strike, the faster the

244   strike, the earlier the detection of the predator (ANCOVA: $F_{2,84} = 5.05$; $P = 0.008$; model: P

245    $= 0.65$; Umax: $P = 0.008$) (Fig. 5).

246
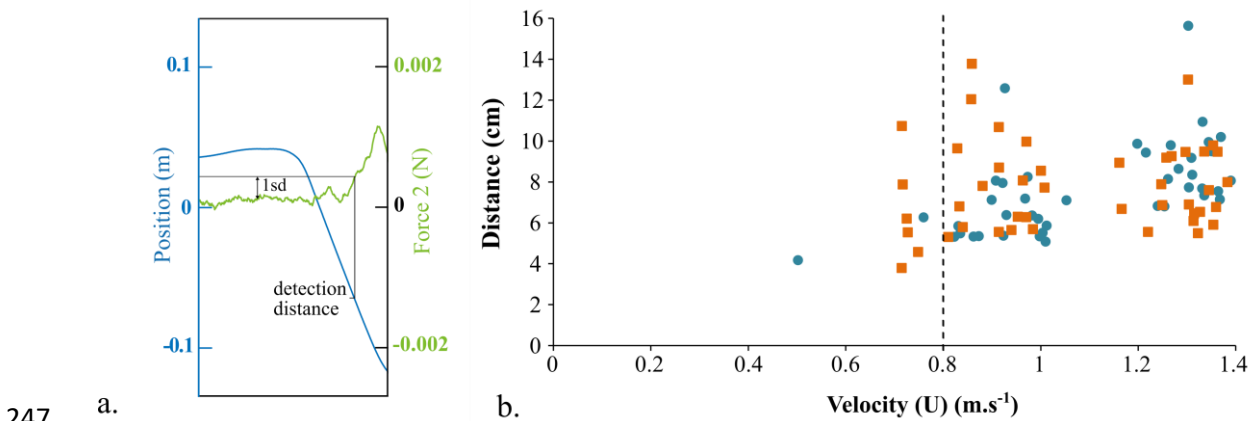
a.   b.

248   *Figure 5: a. Zoom on the prey sensor output highlighting the method used to determine*

249   *the detection distance, using the 1sd (standard deviation) threshold (not at scale here). b.*

250   *Distance (cm) at which the prey could potentially detect the snake depending on the*

251   *maximal velocity of the strike (m.s^{-1}). For each graph: squares: non-aquatic model,*

252   *circles: aquatic model.*

253   *Flow characterization*

254   The frontal strike maneuver involves strong flow separations due to the high shear

255   produced by the impulsive acceleration. The flow features can be characterized by

256   examining the vortex structures formed at the corner of the mouth and on both tips of the

257   jaw and of the skull. We created videos of the vortex formation during a strike, obtained

258   from PIV in three planes around the snake heads (see Materials and Methods section), to

259   compare both models (see Supplementary videos S2-4). The PIV measurements show the

11

260 formation of vortices during the strike maneuver. In Fig. 6a, we compare the vorticity field

261 at the end of the acceleration phase (at t ≈ 0.8 s) in the three measurement planes; bottom

262 view, jaw view, and skull view (Supplementary Fig. S1) for the aquatic and non-aquatic

263 heads. Looking at the bottom view, the advantage of the aquatic model seems to be related

264 to a smaller primary vortex. The picture is not as straightforward considering the jaw and

265 skull view, where opposite observations on the primary vorticity production can be observed

266 qualitatively: on the jaw view the primary vorticity patch appears more detached from the

267 jaw in the non-aquatic case, whereas in the skull view the same is true for the aquatic case.

268 Fig. 6b shows the quantitative analysis of the primary circulation. First, we can see that in

269 the bottom view the aquatic model induces a slightly (~10%) lower overall circulation over

270 the whole acceleration phase. Second, for the jaw view it can be remarked that a much lower

271 overall circulation is produced by the vorticity detached from the tip of the jaw in the aquatic

272 case (around 40% of the non-aquatic value at the end of the acceleration phase). The picture

273 in the skull view is the opposite with the aquatic shape generating more overall circulation

274 but the difference between the two models is less important than for the jaw view. We note

275 also for the skull view that the computed value for the circulation is more variable.
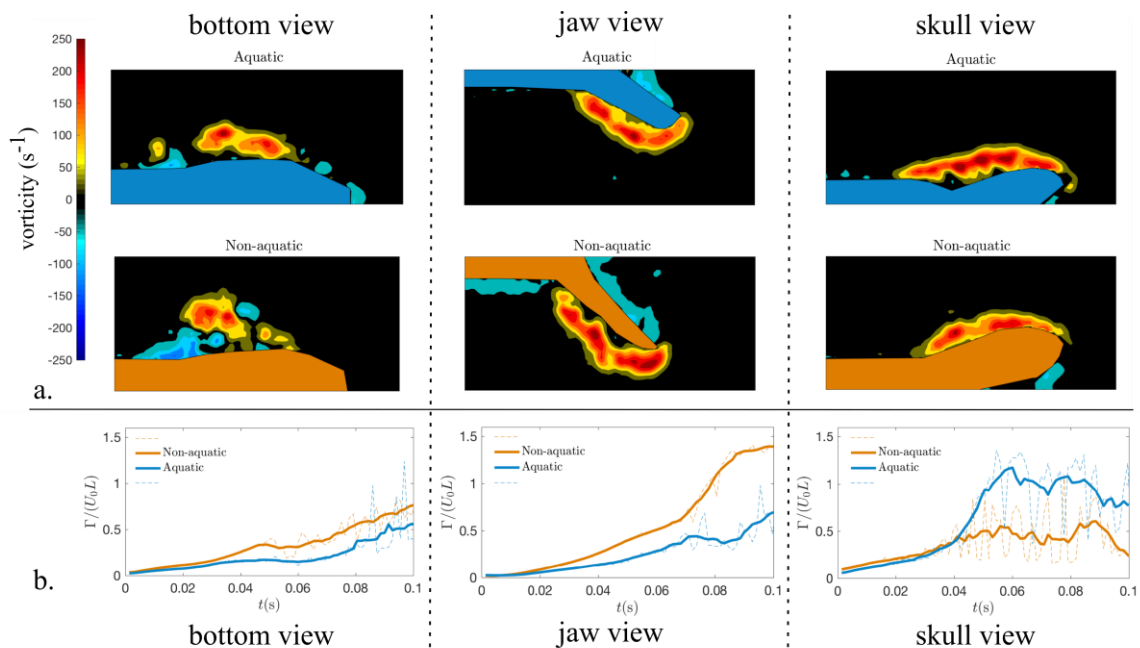
276

Figure 6: a. Snapshots of the vorticity field ωz around the snake head models at the end

of the acceleration phase for the aquatic (first line) and non-aquatic (second line) models,

in the three measurement planes: bottom, jaw and skull views are shown on the first to

third columns, respectively. The color bar for the vorticity field is given in s⁻¹. b. Evolution

12

281   *of the dimensionless integrated positive circulation during the acceleration phase*

282   *depending on the time for both models in each of the three views considered.*

Discussion

284   Drag is well known for its importance during steady locomotion. However, it is also

285   involved in transient behaviors such as the capture maneuver studied here. Certainly, the

286   aquatic shape appears better adapted to capture aquatic prey using a frontal strike than the

287   non-aquatic shape in terms of drag. The aquatic model has a drag coefficient that is almost

288   3 times smaller than the non-aquatic model. As mentioned above, drag in this fast-impulsive

289   maneuver is mainly pressure drag, which is intimately linked to the flow separation in the

290   near wake of the snake head as it moves. The PIV measurements illustrate the vortices that

291   are formed very early during the strike (see Supplementary videos S2-4). Looking at the

292   bottom view in Fig. 6, the drag advantage of the aquatic model could be related to a smaller

293   primary vortex, the non-aquatic case showing a more fluctuating and disordered flow field.

294   Moreover, the vorticity produced at the tip of the jaw shows a clear quantitative difference

295   and is consistently higher for the non-aquatic model. However, the skull view shows the

296   opposite pattern of vorticity; the non-aquatic shape produces fewer vortices with an

297   integrated primary circulation that is less important than for the aquatic model. It should be

298   noted that the 2D nature of the PIV measurements presented here does not allow us to

299   provide a quantitative link between drag and the vorticity profile of the flow around the head.

300   Nonetheless, from the present results we can conjecture that a reduction of the recirculation

301   bubble behind the jaw may be one of the main physical mechanisms explaining the physical

302   advantage of the head shape observed in aquatically foraging snakes.

303   Transient maneuvers under water, such as the underwater prey capture in snakes,

304   implicate an acceleration phase that not only involves drag but also inertia. Inertial forces

305   under water are associated with the mass of the object but also with a mass of the fluid that

306   is accelerated. Thus, the relationship between inertia and shape is not straightforward.

307   However, some studies suggested that an optimal body shape for transient propulsion, such

308   as a snake strike, would be an elongated, streamlined, and flexible body and non-muscle

309   mass reduction, which corresponds to a snake-like configuration [1,17]. To our knowledge, no

310   study to date has focused on the shape of the head and its role. In this study, we highlight

311   that the hydrodynamic forces associated with a transient maneuver are important in

312   comparison with drag (e.g. the peak of force in comparison with the plateau on Fig. 2).

313   Moreover, we demonstrated that the aquatic shape allows to reduce the added mass and is

314   associated with a smaller added mass coefficient. This suggests that drag is not the only

315   driver of the evolution of head shape in aquatic snakes. Moreover, added mass and drag

316   optimization do not require divergent morphological features in the case of aquatic snake

317   strikes, unlike what suggested for the body shape of fish [17].

318   Regarding the prey detection distance, our results show that this distance does not

319   depend on the snake head shape, but rather that it increases with strike velocity. However,

320   we cannot conclude on the biological relevance of the absolute prey detection distance

321   measured in our experiment as our setup was built with as primary purpose to measure drag

322   and added mass. Snakes usually strike when the prey is close to their head (e.g. 0.5-0.8 cm

323   for *Erpeton tentaculatum* [32]; 4.87 cm for *T. couchii*; 2.81 cm for *T rufipunctatus* [33]; less than

324   3 cm for *Hydrophis schistosus* [34]). The detection distance measured here is around 6 to 10

325   cm, so we could consider that the prey can possibly detect the snake almost instantaneously

326   upon the strike initiation, the reaction time of a fish being around 7 ms [32]. Capture success

327   is thus more likely determined by the hydrodynamic profile of the snake head than being

328   dependent on the reaction of the prey.

329   In conclusion, we investigated the role of head shape on the hydrodynamic forces

330   generated by a predator using an experimental approach focusing on a transient maneuver.

331   We were able here to quantify the role and impact of head shape in the hydrodynamics of

332   prey capture in aquatic snakes. We highlighted a clear hydrodynamic advantage of the

333   aquatic head shape when capturing a prey being associated not only with a smaller drag

334   coefficient but also a smaller added mass coefficient. These results validate the hypothesis

335   that the morphological convergence of the head shape in aquatic snakes is an adaptation to

336   an aquatic lifestyle as it provides a clear hydrodynamic advantage. In this work, we focused

337   on the shape of the head of aquatically foraging snakes, as several studies have highlighted

338   convergence therein, and as shape plays a crucial role in the hydrodynamic constraints as

339   well. Size could be an important feature regarding the hydrodynamic constraints. However,

340   we did not detect any allometry in our morphological study, meaning that the aquatically

341   foraging snakes are not significantly different in size than their closely related non-aquatic

342   species. Thus, the present work focuses on the functional meaning of shape irrespective of

343   size. The other factors that could play a role in the hydrodynamics of the prey capture of

344   aquatic snakes could be the gape angle and macro and microscopic skin features which

345   remains to be investigated.

14

346   **References**

347   1.   Webb, P. W. Simple physical principles and vertebrate aquatic locomotion. *Integr.*
348   *Comp. Biol.* **28,** 709–725 (1988).

349   2.   Vogel, S. *Life In Moving Fluids: The Physical Biology Of Flow*. (Princeton
350   University Press, 1994).

351   3.   Hoerner, S. F. *Fluid Dynamic Drag*. (Hoerner Fluid Dynamics, 1965).

352   4.   Godoy-Diana, R. & Thiria, B. On the diverse roles of fluid dynamic drag in animal
353   swimming and flying. *J. R. Soc. Interface* **15,** 20170715 (2018).

354   5.   Daniel, T. L. Unsteady aspects of aquatic locomotion. *Am. Zool.* **24,** 121–134
355   (1984).

356   6.   Brennen, C. E. A review of added mass and fluid inertial forces. (1982).

357   7.   Bilcke, J., Herrel, A. & Aerts, P. Effect of prey and predator size on the capture
358   success of an aquatic snake. *Belgian J. Zool.* **137,** 191–195 (2007).

359   8.   Kelley, N. P. & Motani, R. Trophic convergence drives morphological convergence
360   in marine tetrapods. *Biol. Lett.* **11,** 5 (2015).

361   9.   Howell, A. B. *Aquatic Mammals*. (Dover Publications Inc, 1971).

362   10.   Winemiller, K. O., Kelso-Winemiller, L. C. & Brenkert, A. L. Ecomorphological
363   diversification and convergence in fluvial cichlid fishes. *Environ. Biol. Fishes* **44,**
364   235–261 (1995).

365   11.   Van Wassenbergh, S. *et al.* Hydrodynamic constraints on prey-capture performance
366   in forward-striking snakes. *J. R. Soc. Interface* **7,** 773–785 (2010).

367   12.   Stayton, C. T. Biomechanics on the half shell: Functional performance influences
368   patterns of morphological variation in the emydid turtle carapace. *Zoology* **114,**
369   213–223 (2011).

370   13.   Young, B. A. The influences of the aquatic medium on the prey capture system of
371   snakes. *J. Nat. Hist.* **25,** 519–531 (1991).

372   14.   Herrel, A. *et al.* Morphological convergence as a consequence of extreme functional

15

373   demands: examples from the feeding system of natricine snakes. *J. Evol. Biol.* **21,**
374   1438–1448 (2008).

375   15.   Hibbitts, T. J. & Fitzgerald, L. A. Morphological and ecological convergence in two
376   natricine snakes. *Biol. J. Linn. Soc.* **85,** 363–371 (2005).

377   16.   Segall, M., Cornette, R., Fabre, A.-C., Godoy-Diana, R. & Herrel, A. Does aquatic
378   foraging impact head shape evolution in snakes ? *Proc. R. Soc. London, B Biol. Sci.*
379   **283,** (2016).

380   17.   Webb, P. W. Body form, locomotion and foraging in aquatic vertebrates. *Am. Zool.*
381   **24,** 107–120 (1984).

382   18.   Esquerré, D. & Keogh, J. S. Parallel selective pressures drive convergent
383   diversification of phenotypes in pythons and boas. *Ecol. Lett.* **19,** 800–809 (2016).

384   19.   Vincent, S. E., Brandley, M. C., Herrel, A. & Alfaro, M. E. Convergence in trophic
385   morphology and feeding performance among piscivorous natricine snakes. *J. Evol.*
386   *Biol.* **22,** 1203–1211 (2009).

387   20.   Fabre, A.-C., Bickford, D., Segall, M. & Herrel, A. The impact of diet, habitat use,
388   and behavior on head shape evolution in homalopsid snakes. *Biol. J. Linn. Soc.* **118,**
389   634–647 (2016).

390   21.   van Netten, S. M. Hydrodynamic detection by cupulae in a lateral line canal:
391   functional relations between physics and physiology. *Biol. Cybern.* **94,** 67–85
392   (2006).

393   22.   McHenry, M. J., Feitl, K. E., Strother, J. A. & Van Trump, W. J. Larval zebrafish
394   rapidly sense the water flow of a predator's strike. *Biol. Lett.* **5,** 477–9 (2009).

395   23.   Thiria, B., Goujon-Durand, S. & Wesfreid, J. E. The wake of a cylinder performing
396   rotary oscillations. *J. Fluid Mech.* **560,** 123–147 (2006).

397   24.   Saffman, P. G. *Vortex Dynamics*. (Cambridge University Press, 1992).

398   25.   Ringuette, M. J., Milano, M. & Gharib, M. Role of the tip vortex in the force
399   generation of low-aspect-ratio normal flat plates. *J. Fluid Mech.* **581,** 453 (2007).

400   26.   Bilcke, J., Herrel, A. & Van Damme, R. Correlated evolution of aquatic prey-

401 capture strategies in European and American natricine snakes. *Biol. J. Linn. Soc.* **88,**
402 73–83 (2006).

403 27. Vincent, S. E., Herrel, A. & Irschick, D. J. Comparisons of aquatic versus terrestrial
404 predatory strikes in the pitviper, Agkistrodon piscivorus. *J. Exp. Zool. Part A Comp.*
405 *Exp. Biol.* **303,** 476–488 (2005).

406 28. Radford, C. A., Montgomery, J. C., Caiger, P. & Higgs, D. M. Pressure and particle
407 motion detection thresholds in fish: a re-examination of salient auditory cues in
408 teleosts. *J. Exp. Biol.* **215,** 3429–3435 (2012).

409 29. Kastelein, R. A. *et al.* Startle response of captive North Sea fish species to
410 underwater tones between 0.1 and 64 kHz. *Mar. Environ. Res.* **65,** 369–377 (2008).

411 30. Moisy, F. A PIV Post-processing and data analysis toolbox : PIVMat 4.00 27 Apr
412 2006 (Updated 26 Apr 2016). (2006).

413 31. R Development Core Team. *R: A language and environment for statistical*
414 *computing.* (2014).

415 32. Catania, K. C. Tentacled snakes turn C-starts to their advantage and predict future
416 prey behavior. *Proc. Natl. Acad. Sci. U. S. A.* **106,** 11183–7 (2009).

417 33. Alfaro, M. E. Forward attack modes of aquatic feeding garter snakes. *Funct. Ecol.*
418 **16,** 204–215 (2002).

419 34. Voris, H. K., Voris, H. H. & Liat, L. B. The food and feeding behavior of a marine
420 snake, Enhydrina schistosa (Hydrophiidae). **1978,** 134–146 (1978).

421 **Acknowledgments**

428 **Author contributions**

429   All authors helped revise and approved the manuscript and conceived the study. MS carried

430   out the data collection, the statistical analyses, and wrote the manuscript. RGD helped to

431   build the experimental setup and to interpret the data. RGD carried out the particle image

432   velocimetry analysis. AH participated in the scientific interpretation of the data in a

433   biological context.

434   **Competing interests**

435   We have no competing interests.

436   **Data availability**

437   See Supplementary Table S5

438   **Figure legends**

439   *Figure 1:* 3D models of the head shape of non-aquatic (left) versus aquatic snakes (right) in

440   front, side and top view.

441   *Figure 2: a.* Experimental setup used to simulate a frontal attack of a snake towards a prey.

442   *b.* Example of the output of the force sensor 1 (red line), force sensor 2 (green dashed line)

443   and velocity (blue line) during one trial (i.e. one strike). The plateau and peak force used to

444   calculate the hydrodynamic forces are indicated.

445   *Figure 3:* Drag term $2F_d/\rho S$ depending on the velocity term of the strike (U^2) for the two

446   head models tested. Linear regression lines are drawn. The slopes correspond to the drag

447   coefficient of each shape and the R^2 are the regression coefficients. Squares: non-aquatic

448   model, circles: aquatic model.

449   *Figure 4:* Normalized inertial force term $(F_i-ma)/\rho V$ depending on the acceleration of the

450   strike (a in $m.s^{-2}$) for the two head models tested. Linear regression lines are drawn. The

451   slopes correspond to the added mass coefficient of each shape and the R^2 are the regression

452   coefficients. Squares: non-aquatic model, circles: aquatic model.

453   *Figure 5: a.* Zoom on the prey sensor output highlighting the method used to determine the

454   detection distance, using the 1sd (standard deviation) threshold (not at scale here). *b.*

455   Distance (cm) at which the prey could potentially detect the snake depending on the maximal

456   velocity of the strike ($m.s^{-1}$). For each graph: squares: non-aquatic model, circles: aquatic

457   model.

458   *Figure 6: a.* Snapshots of the vorticity field ω$_z$ around the snake head models at the end of

459   the acceleration phase for the aquatic (first line) and non-aquatic (second line) models, in the

460   three measurement planes: bottom, jaw and skull views are shown on the first to third

461   columns, respectively. The color bar for the vorticity field is given in s−1. *b.* Evolution of

462   the dimensionless integrated positive circulation during the acceleration phase depending on

463   the time for both models in each of the three views considered.